

Commercial RFIDs as Reconfigurable Intelligent Surfaces

Jingyu Tong[†], Xiaopeng Zhao[†], Zhicheng Wang[†], Donghui Dai[†], Zhenlin An[‡], Lei Yang^{†§*}

[†]Department of Computing, The Hong Kong Polytechnic University

[‡]Department of Computer Science, University of Pittsburgh

[§]Shenzhen Research Institute, The Hong Kong Polytechnic University

Email: {jerry.tong, xiaopeng.zhao, zhicheng0603.wang, donghui.dai}@connect.polyu.hk, {an, young}@tagsys.org

Abstract—Reconfigurable Intelligent Surfaces (RISs) are emerging as cost-effective solutions for enhancing signal transmission in wireless networks. Traditional RIS designs, however, face challenges such as bulkiness, high production costs, limited scalability, and intricate installation due to their reliance on wired connections. In this work, we innovate by repurposing 920MHz RFID tags into battery-free unit cells, creating an affordable, scalable, and flexible one-bit phase-modulated RIS. This novel system, referred to as MetaMosaic, is engineered for compatibility with 2.4GHz Wi-Fi communications while being controlled at a 920MHz frequency. Our approach is distinguished by two primary innovations: the conversion of RFID tags into functional unit cells, and the development of a bespoke neural radiance field to identify the most effective reconfiguration strategy. We constructed six MetaMosaic surfaces, each comprising 403 cells, using a total of 2,418 repurposed RFID tags at a cost of 50 cents per tag. Our extensive testing in ten varied environments demonstrates that MetaMosaic substantially boosts signal strength, achieving a mean of 19dB gain (i.e., 80×) over non-RIS setups. This outperforms current leading RIS systems by a 3-fold improvement. In the context of XR application, the field study showcases a more than doubling of throughput and a halving of latency.

Index Terms—reconfigurable intelligent surfaces, RFID, neural radiance field

I. INTRODUCTION

Reconfigurable Intelligent Surfaces (RISs) are a groundbreaking development in the realm of wireless communication, responding to the critical need for improved network efficiency and capacity in an era of increasing connectivity. These innovative surfaces, capable of actively modifying the behavior of electromagnetic waves, are reshaping wireless network operations [1], [2], [3], [4]. The purpose of RISs extends to redefining network infrastructure, paving the way for more sustainable, adaptable, and efficient solutions, particularly crucial in the rollout of 5G networks and beyond. In essence, RISs are a response to the growing demands and complexities of wireless communication, offering a novel approach to meet these challenges head-on.

Nevertheless, the realization of a scalable, minimally burdensome, and economically viable RIS faces significant challenges. First, the prevalent designs of RIS are typically tailored to specific use cases with specialized unit cells, which

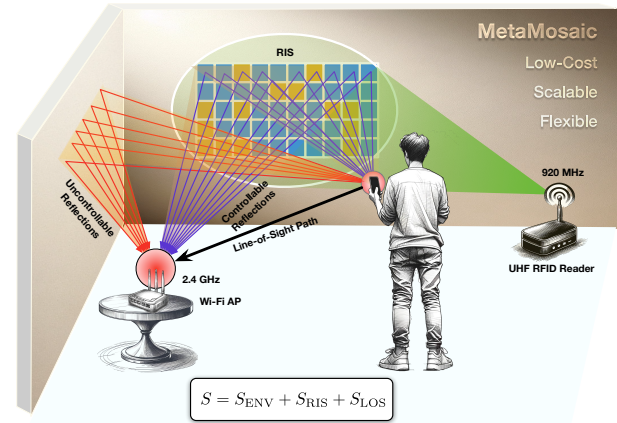


Fig. 1: Usage Scenario. The Wi-Fi AP or mobile device captures RF signals through direct line-of-sight propagation, uncontrollable reflections from the surrounding environment, and controlled reflections from the RIS. The goal of our system is to use UHF RFID tags to create a cost-effective, scalable, and adaptable RIS. This system is energized and managed by a remote RFID reader.

limits their scalability in terms of production and cost. The lack of standardization precludes these systems from reaping the benefits of mass production, consequently escalating the manufacturing costs. Secondly, the current design paradigm of RIS often involves wired connections between the unit cells and the centralized controller. This wired framework imposes a constraint on scalability, particularly in terms of the number of unit cells that can be feasibly integrated. Lastly, the operation of RIS systems necessitates a power source to sustain the operational parameters of its unit cells. However, the maintenance expenses for such power requirements become prohibitively high, especially in the context of an extra-large RIS. This creates a substantial economic burden, further complicating the spread of RIS systems.

As one of the earliest and most well-established backscatter communication systems, RFIDs alternate their internal impedance between two states — reflective and non-reflective — to relay information to a reader. This fundamental communication method uniquely positions RFID as the minimal unit for a one-bit reflective RIS. When “on”, the RIS reflects the signal; otherwise, the signal is absorbed. Inspired by

*Lei Yang is the corresponding author.

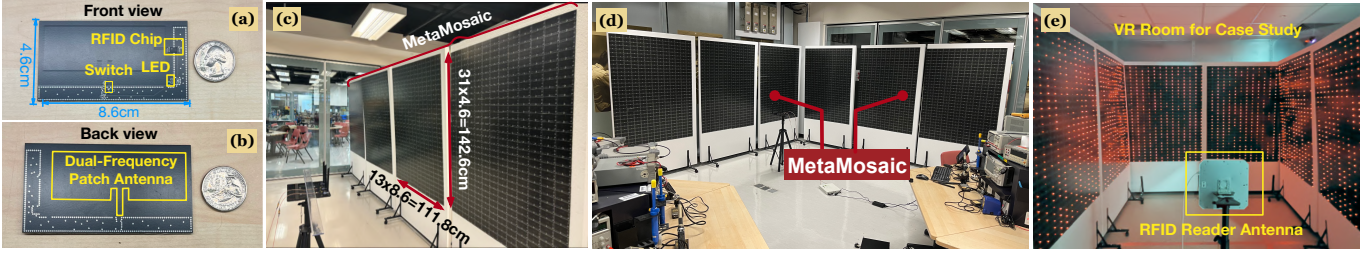


Fig. 2: Prototypes of MetaMosaic. (a) and (b) the unit cells, which are constructed from RFID tags, seen from the front and back, respectively. (c) and (d) illustrate the surfaces of MetaMosaic, each arranged with a grid of 13×31 unit cells. (e) displays a practical application within a VR room, an enclosed area encircled by six MetaMosaic surfaces. The unit cells lit by LEDs have been designated to flip the phase of the reflected EM waves by 180° , while the remaining unit cells reflect unaltered waves.

this insight, we can employ a collective array of RFID tags to construct a large-scale RIS, on which each RFID tag, functioning as an individual unit cell, is wirelessly controlled by a remote RFID reader.

We term our innovative Reconfigurable Intelligent Surface as MetaMosaic, termed after the intricate art of mosaic. MetaMosaic is an assembly of numerous individual RFID tags, collectively forming an expansive and unified surface. MetaMosaic stands out by innovatively converting commercially available passive RFID tags into dynamic unit cells to forge a one-bit, phase-modulated reflective RIS. As depicted in Fig. 1, the MetaMosaic setup is strategically mounted on a wall. It operates under the control of a distant RFID reader, functioning at a frequency of 920MHz. Concurrently, MetaMosaic possesses the capability to reflect incoming electromagnetic waves at 2.4GHz, either maintaining their phase or introducing a 180-degree phase shift. This selective phase modulation enables the controllable reflections to synchronize in phase with the aggregate signal derived from various paths, enhancing overall signal coherence and efficacy. This approach not only redefines the application of RFID technology but also paves the way for more adaptable and efficient wireless communication environments.

MetaMosaic offers a new direction in RIS design with notable advantages. (1) *Cost-Effectiveness*: It uses mass-produced UHF RFID chips to reduce costs to under 50 cents per unit. (2) *Flexibility*: The wireless nature allows for versatile and straightforward deployment. (3) *Scalability*: Its wireless framework facilitates seamless scale-up, embracing expansive and intricate environments without the limitations of wiring. (4) *Efficiency*: Units operate with Gen2 RFID tags for simultaneous control, improving responsiveness. (5) *Sustainability*: Battery-free design ensures lower operational and maintenance costs, making it an eco-friendly solution.

However, adapting MetaMosaic for practical, real-world applications presents two primary challenges:

- First, UHF RFID systems generally function at around 920MHz, restricted to a narrow bandwidth of 20MHz, which results in less efficient reflection at the target 2.4GHz band. To bridge this gap, we re-engineered a dual-frequency microstrip patch antenna for each RFID-addressed unit cell to achieve two main goals. The first is to optimize these antennas to efficiently harvest energy and receive signals from a 920MHz

RFID reader's continuous wave. The second is to adapt these antennas to effectively reflect RF signals at 2.4GHz or above, thereby aiding corresponding frequency wireless communication.

- Second, a crucial feature of a RIS is its ability to reconfigure the reflective coefficients of its unit cells, thus orchestrating constructive interference of signals at the receiver's location. In a one-bit RIS that includes M elements, the number of possible states for the system can reach 2^M , giving rise to a vast array of configuration possibilities. This complexity has led to the reliance on heuristic algorithms in earlier systems, which incrementally adjust configurations using immediate feedback from mobile devices, such as variations in RSS [2]. This hard-landing approach, while effective, can be time and energy-intensive. To mitigate this issue, we propose the creation of a specialized neural radiance field for RIS, designated as RIS-NeRF². This framework would undergo pre-training through a finite collection of RF measurements. It is designed to swiftly pinpoint the optimal RIS configuration parameters, streamlining the reconfiguration protocol, and thereby elevating the system's efficacy and operational performance.

Summary of Results: We developed six MetaMosaic surfaces by using a total of 2,418 unit cells, as shown in Fig. 2. The demo can be found at <https://youtu.be/i6h5oVHsSt4>. Our comprehensive evaluation in ten diverse settings, ranging from real-world office spaces to laboratory rooms, yielded the following insights:

- The RIS-NeRF² model consistently achieved an average median deviation of just 0.74% in signal prediction, exemplifying its high accuracy. This precision forms the cornerstone for employing a soft-landing algorithm for optimal reconfiguration, substantially reducing the reconfiguration time to merely one-tenth of that required by traditional hard-landing methods.
- Across the ten different scenes, MetaMosaic realized an average median gain of 18.82dB, peaking at a median gain of 25dB. This performance notably surpasses existing state-of-the-art large-scale RIS by an additional 8.51dB. The system's adaptability was also demonstrated, proving its effectiveness as a general-purpose RIS solution and scalability in different settings and layouts.
- In virtual reality (VR)-based field study, where an enclosed space was surrounded by MetaMosaic surfaces, the system

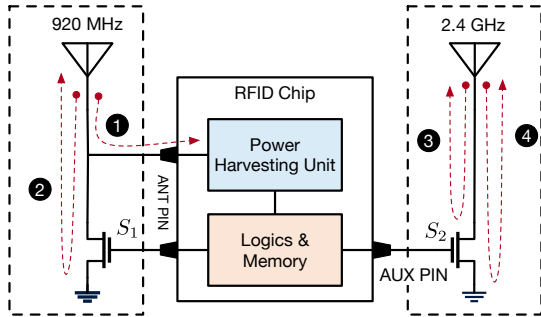


Fig. 3: Design of the unit cell. The unit cell of MetaMosaic is composed of a commercial RFID chip and two antennas operating at 920MHz and 2.4GHz, respectively.

facilitated a data throughput of 14.86Mbps and 4.63ms, showcasing its practical application and effectiveness in a controlled, immersive environment.

II. REPURPOSING RFID INTO UNIT CELL

This section begins with an introduction to the fundamentals of RFID technology and then progresses to explain how an RFID tag can be converted into a unit cell.

A. RFID Background

In Ultra-High-Frequency (UHF) RFID systems, a device known as the reader emits a strong RF signal. Nearby RFID tags detect and respond to this emitted signal. Each RFID tag comprises two primary components:

- **Microchip:** The heart of the tag, storing data like the unique EPC and possibly other information. Its memory can be read-only or writable, and it controls tag operations.
- **Antenna:** Specifically designed for UHF frequency operation, the antenna draws energy from the reader's signal to power the microchip, negating the need for a battery.

An RFID tag represents the simplest instance of a one-bit RIS, functioning as a solitary unit. Benefiting from the economies of scale, with around 40 billion UHF tags reportedly sold in 2023 [5], the per-unit cost of these tags has significantly reduced, currently standing at as low as 5 cents. This widespread adoption and mass production have contributed to making RFID tags more affordable.

B. From Tag To Unit Cell

Microchips and antennas are typically produced by separate manufacturers in the market. These components are then combined by downstream suppliers for various applications. Following this practice, the unit cell of MetaMosaic incorporates two antennas into existing commercial microchips, as shown in Fig. 3.

The first antenna, situated on the left, is tuned to a frequency of 920MHz. It interfaces with an impedance switch, labeled S_1 , alongside a power harvesting module. This switch is regulated by the RFID's internal logic and toggles between two modes:

- **Absorptive State.** When the switch S_1 is off, it renders an open circuit. With the power harvesting unit's input

impedance tailored to the antenna's, it allows the inbound signal to penetrate the circuit, optimizing power absorption. In this state, the cell primarily functions as an energy absorber.

- **Reflective State.** When the switch S_1 is on, it creates a closed circuit, effectively grounding the antenna. This disrupts impedance matching, resulting in the complete reflection of the incident RF signal.

By default, the antenna's principal role is to gather energy or accept instructions from an external reader.

The second antenna, situated on the right, operates at 2.4GHz. It is linked directly to ground through an additional impedance switch S_2 . This switch offers a separate backscattering mechanism. Unlike the 920MHz configuration, the RF signals in this subsystem do not enter the chip but are reflected constantly. The corresponding reflection coefficient is described by:

$$\Gamma = \frac{Z_L - Z_A}{Z_L + Z_A} \quad (1)$$

where Z_L represents the impedance when the switch is engaged, and Z_A denotes the antenna's impedance at 2.4GHz. The logic system governs the switch S_2 , resulting in two distinct configurations:

- **Open-Circuit Configuration:** When the switch S_2 off, the switch circuit's impedance, Z_L , effectively becomes infinite. As a result, the reflection coefficient reaches a maximum value of 1, i.e., $\Gamma = \frac{\infty - Z_A}{\infty + Z_A} = 1$. This causes the incident RF signals to be completely reflected by the 2.4GHz antenna, with no alteration in phase.

- **Short-Circuit Configuration:** Conversely, when the switch S_2 is closed, the switch circuit's impedance, Z_L , to approximately zero, indicating a short-circuit condition. The reflection coefficient then becomes $\Gamma = \frac{0 - Z_A}{0 + Z_A} = -1 = e^{j\pi}$. Under these circumstances, the incident wave S is fully reflected with a phase shift of π , as $Se^{j\pi}$, implying a 180-degree phase change.

Therefore, the reflective coefficient of a unit cell Γ at 2.4GHz is either 1 or -1. Our unit cell effectively functions as a one-bit RIS, capable of phase modulation on the incoming signals.

C. Controlling Reflective Coefficients

The logic circuits within an RFID chip are designed to adhere to the EPCglobal Gen 2 air protocol [6] only. So, how can we harness a commercial RFID chip to control the 2.4GHz reflection coefficient? As demand increases, more RFID chips nowadays provide additional pins that can output the tag's internal state. Take for instance, the EM4325 chip from EM Microelectronic [7], which includes an AUX pin capable of indicating the tag's status as either selected or not-selected as per the Gen2 protocol stipulations. Prior to commencing the inventory process, an RFID reader can employ a Select command to enlist specific tags for participation. A high voltage signal from the AUX pin indicates the selection of the tag, while a low voltage denotes its non-selection. As shown in Fig. 3, we connect this AUX pin to the switch

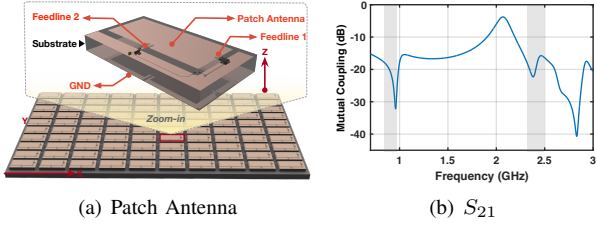


Fig. 4: Dual-frequency patch antenna. (1) we leverage the dual polarization of path antenna at the two edges to achieve the dual-frequency antenna. (2) shows the mutual coupling coefficient S_{21} of two feed ports.

S_2 . Consequently, changing the reflection coefficient turns out to be a selection problem – the selected state triggers the opening of switch S_2 ; if not selected, the switch remains off. Consequently, we can use a simple Select command to change the reflection coefficients of unit cells.

D. Dual-Frequency Patch Antenna

While it might appear that incorporating two antennas would necessitate additional space, in reality, the microstrip patch antenna is innately capable of resonating and emitting at two distinct frequencies, f_1 and f_2 , along its two edges, respectively. As Fig. 4(a) shows, the resonant frequencies of the antenna are highly dependent on its height H and width W . Formally, $f_1 = \frac{c}{2H\sqrt{\epsilon_e}}$ and $f_2 = \frac{c}{2W\sqrt{\epsilon_e}}$, where c is the speed of light and ϵ_e is the effective dielectric constant. Notably, each frequency is characterized by a different polarization direction, orthogonal to each other. By attaching two feedlines to distinct edges of the patch antenna, it is possible to utilize both frequencies simultaneously without mutual interference. In our configuration, dimensions of $W = 8.6\text{cm}$ and $H = 4.6\text{cm}$ have been selected to facilitate operation at frequencies of 920MHz and 2.4GHz, respectively. Fig. 4(b) illustrates the mutual coupling (S_{21}) between two feed ports. As it can be seen, at the two operational bands, the coupling coefficient remains below -15dB, indicating a mere 0.3% energy transfer from one port to the other. Consequently, this design permits the modulation of the phase of the 2.4GHz signal without affecting the 920MHz signal state. This design strategy enables the antenna to maintain a size that is on par with conventional RFID tags despite its dual-frequency functionality.

III. RIS RECONFIGURATION

In this section, we take advantage of neural radiance fields to optimize the reconfiguration algorithm.

A. Hard-landing Reconfiguration

The primary objective of RIS is to modify surface reflections in a manner that allows controllable reflections to constructively align with the LoS propagation at the receiver, thereby enhancing the signal strength. This process necessitates the mobile device to constantly provide feedback on signal strength each time there is a shift in the RIS configuration. This method of collaborating with the mobile device to evaluate the effectiveness of a RIS configuration is

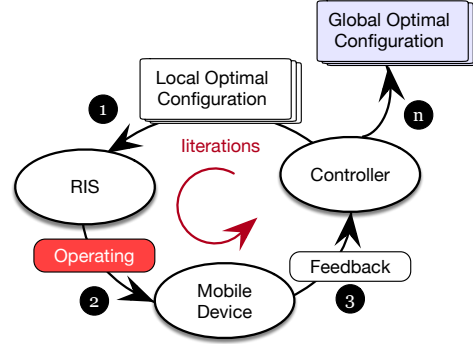


Fig. 5: Hard-landing based Configuration strategy. Past RIS systems adopt the heuristic search algorithm to identify the optimal configuration parameters after multiple iterations. In each iteration, when a new configuration is assumed, the controller necessitates the RX device to constantly provide feedback on the signal strength.

termed “hard landing”, as shown in Fig. 5. Notably, the hard landing is laborious and time-intensive. This is not only due to the nature of the feedback acquisition but also because of a staggering 2^M potential configurations for a M -cell RIS. Traditional RIS systems often lean on heuristic algorithms for the optimization of reconfiguration [2], [8], which necessitates multiple iterations to ascertain the optimal configuration.

B. Scene Representation

The necessity for a “hard landing” in reconfiguration arises from the inability to accurately predict channel behavior. To tackle this issue, it’s crucial to develop a model for the current scene that enables a more refined, “soft-landing” reconfiguration approach, which can effectively simulate the performance of a proposed configuration. This concept is inspired by the neural radiance fields (NeRF) [9], a technique designed for the detailed modeling of complex 3D scenes. Extending NeRF’s principles, NeRF² broadened its scope from the optical realm to encompass electromagnetic aspects, particularly for simulating radio-frequency radiance fields [10]. In line with these developments, we introduce RIS-NeRF² to represent the scene where the RIS operates. This model breaks down the scene into a myriad of small, continuous voxels, each characterized by a 3D coordinate and two critical properties: attenuation and radiance properties.

• **Attenuation Property:** Each voxel V_i full of air or other medium attenuates the propagation of the RF signals that travel through the voxel. The attenuation property of voxel V_i is quantified as a complex number denoted by $h(V_i)$:

$$h(V_i) = \Delta a(V_i) e^{j\Delta\theta(V_i)} \quad (2)$$

where $\Delta a(V_i)$, normalized between 0 and 1, indicates amplitude reduction, while $\Delta\theta(V_i)$, ranging from 0 to 2π , represents the phase shift. To facilitate computation, this coefficient is usually converted into a negative logarithmic form denoted by $\delta(V_i)$:

$$\begin{aligned} \delta(V_i) &= -\ln(h(V_i)) = -\ln(\Delta a(V_i) e^{j\Delta\theta(V_i)}) \\ &= -\ln \Delta a(V_i) - j\Delta\theta(V_i) \end{aligned} \quad (3)$$

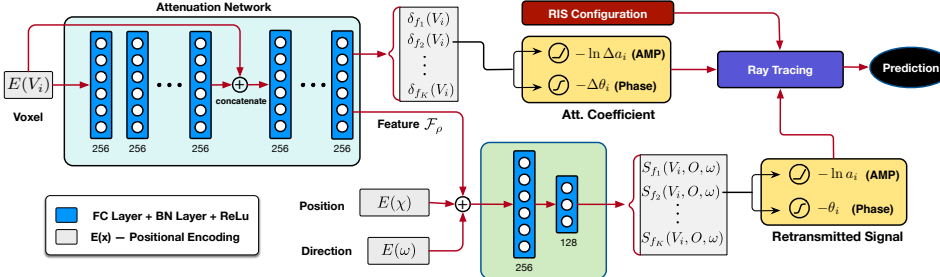


Fig. 6: Network Architecture of RIS-NeRF²

The use of negative logarithms allows for easier confinement of these ranges through the application of ReLU and Sigmoid functions in the neural network layers.

- **Radiance Property:** Guided by the Huygens-Fresnel principle, each voxel within a scene becomes an auxiliary source of radiance when it encounters incoming signals. We envision this scenario as each voxel V_i re-radiating RF signals. The process of this re-emission is encapsulated as follows:

$$S(P_{\text{TX}}, V_i, \omega) = a(V_i)e^{j\theta(V_i)} \quad (4)$$

where P_{TX} signifies the TX's location, and ω represents the direction in which the signal is re-emitted. The terms $a(V_i)$ and $\theta(V_i)$ denote the initial amplitude and phase of the signal emitted by voxel V_i , respectively. The emission direction ω is defined as a two-dimensional variable, including the azimuthal and elevation angles. This mathematical representation implies that the RF signals are re-emitted by the voxel V_i toward the direction ω , considering the TX's position at P_{TX} . By adopting this model, we can abstract the intricate and complex interplays and radiative properties of voxels within the scene. Such an abstraction is pivotal for an in-depth and accurate analysis of RF signal propagation patterns and behaviors, enhancing our understanding of signal dynamics within various environmental contexts.

C. Neural Radiance Fields

How could we estimate the two properties of each voxel? Following the practice of NeRF², we also use two MLPs (called RIS-NeRF²) to model the attenuation and radiance properties of a voxel, as shown in Fig. 6. Specifically, one MLP called *attenuation network* is to model the attenuation property of a voxel, while the other one called *radiance network* is to model the radiance property.

- **Attenuation Network.** This network, symbolized as F_δ , takes the 3D coordinates of a voxel $V_i(x_i, y_i, z_i)$ and computes both the attenuation coefficient $\delta(V_i)$ and a feature vector $F(V_i)$. The formulation is as follows:

$$F_\delta : (V_i) \rightarrow (\delta(V_i), F(V_i)) \quad (5)$$

The output includes the attenuation coefficient $\delta(V_i)$, a complex number, and a 256-dimensional feature vector $F(V_i)$. The real part of $\delta(V_i)$ is refined using a ReLU activation function, ensuring that $-\ln(\Delta a(V_i)) \geq 0$. The imaginary part is modified with a $2\pi \times$ sigmoid function to limit the phase shift

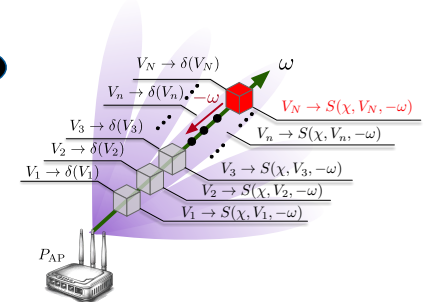


Fig. 7: Ray Tracing

within 0 to 2π . The feature vector $F(V_i)$, processed through eight fully connected layers with ReLU activations and 256 channels, then serves as input to the radiance subnetwork. Notably, the attenuation characteristic is dictated by the voxel's intrinsic density and the structural makeup of the scene, making it independent of the incoming RF signals.

- **Radiance Network.** Represented by F_Y , this subnetwork predicts the properties of the RF signal re-emitted by a voxel. Its input parameters include the voxel's attenuation feature vector $F(V_i)$, the observation direction ω , and the TX's position P_{TX} . The subnetwork's role is described by:

$$F_Y : (P_{\text{TX}}, F(V_i), \omega) \rightarrow a(V_i)e^{j\theta(V_i)} \quad (6)$$

The radiance subnetwork, comprising two fully connected layers with ReLU activations (256 channels in the first layer and 128 in the second), outputs the direction-dependent re-emitted RF signal $a(V_i)e^{j\theta(V_i)}$. The amplitude $a(V_i)$ and phase $\theta(V_i)$ components of this signal are also fine-tuned using ReLU and Sigmoid activation functions, respectively.

D. Ray Tracing

To utilize RIS-NeRF² for forecasting the RF signal received at the AP, we employ a divide-and-conquer strategy in our ray tracing methodology. As illustrated in Fig. 7, the RF signal reception at the AP is systematically deconstructed. In particular,

- ❶ the total RF signal is a synthesis of contributions from all possible directions
- ❷ the RF signal from any given direction is a cumulative result of signals emanating from all voxels along that directional path
- ❸ the signal re-emitted from each individual voxel on the path. By tracing and incrementally integrating these individual voxel signals, we can accurately estimate the final signal that the AP receives.

- **Tracing from a Single Voxel.** As Fig. 7 shows, our objective is to ascertain the contribution of voxel V_N to the RF signal at the AP. We establish a ray trajectory from the AP targeting V_N . This ray, oriented along ω , intersects a sequence of $N - 1$ voxels, denoted as V_1, V_2, \dots, V_{N-1} , with V_1 closest to the AP and V_{N-1} at the furthest extent. The signal re-emitted by voxel V_N is represented as $S(\chi, V_N, -\omega)$, which is derived from the radiance network F_Y . This signal represents the RF output from V_N directed oppositely to ω . This signal undergoes attenuation due to the presence of voxels $\{V_{N-1}, V_{N-2}, \dots, V_1\}$ situated between the AP

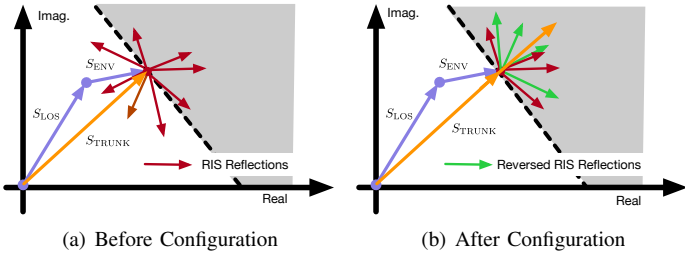


Fig. 8: Configuration Strategy. The orientations of reflections from the unit cells of the RIS are maintained or reversed to ensure alignment with the primary trunk signal

and V_N . Therefore, the final RF signal received by the AP, contributed by voxel V_N , is articulated as follows:

$$\begin{aligned} S(\chi, V_N) &= \left(\prod_{m=1}^{N-1} h(V_m) \right) \cdot S(\chi, V_N, -\omega) \\ &= \exp \left(- \sum_{m=1}^{N-1} \delta(V_m) \right) \cdot S(\chi, V_N, -\omega) \end{aligned} \quad (7)$$

• **Tracing from a Direction.** The process of signal tracing can be expanded from a single voxel to encompass the entire directional path by aggregating the RF signals transmitted from each voxel along that path. Consequently, the signal received from a specific direction ω can be reformulated as:

$$\begin{aligned} S(\chi, \omega) &= \sum_{n=1}^N S(\chi, V_n) \\ &= \sum_{n=1}^N \left(\exp \left(- \sum_{m=1}^{N-1} \delta(V_m) \right) \cdot S(\chi, V_n, -\omega) \right) \end{aligned} \quad (8)$$

where V_N at the furthest extent of the scene. Every voxel on the path functions simultaneously as a secondary source of RF radiation and as an obstacle that impedes the passage of RF signals traversing it.

• **Tracing from All Directions.** The AP is capable of capturing RF signals originating from all voxels within the scene. Nevertheless, computing the signal contributions from each voxel across the whole scene is computationally demanding. To manage this, we typically trace a discrete subset of potential directions to estimate the final RF signal received by the AP as follows:

$$\begin{aligned} S(\chi) &= \sum_{\omega \in \Omega} S(\chi, \omega) = \sum_{\omega \in \Omega} \sum_{n=1}^N S(\chi, V_n) \\ &= \sum_{\omega \in \Omega} \sum_{n=1}^N \left(\exp \left(- \sum_{m=1}^{n-1} \delta(V_m) \right) \cdot S(\chi, V_n, -\omega) \right) \end{aligned} \quad (9)$$

where Ω represents the set of all potential directions from which signals can be received. By summing over these directions, the AP effectively compiles a comprehensive picture of the RF landscape, capturing signals from every voxel along each path. As aforementioned, the Wi-Fi signals contain multiple orthogonal subcarriers. Thus, the ray tracing must be performed at these subcarriers respectively.

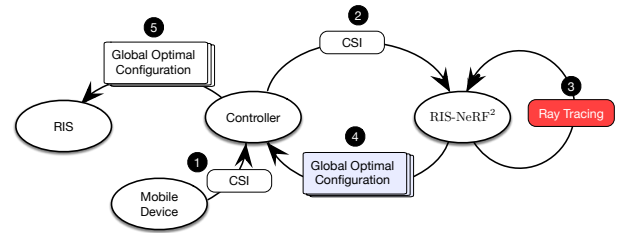


Fig. 9: Soft-landing based Configuration. The efficacy of a proposed configuration can be evaluated by the ray tracing algorithm with RIS-NeRF². This approach allows for the assessment of the configuration’s impact without actually implementing it on the RIS or necessitating feedback from the TX.

E. Training

RIS-NeRF² is developed to create a model of the scene. Once the dual MLPs are effectively trained, forecasting the RF signals becomes feasible. For this purpose, it is necessary to compile a set of CSI data, gathered by positioning the mobile device at N distinct locations within the scene. The training objective is to minimize the following loss function:

$$\mathcal{L} = \frac{1}{N} \sum_{i=1}^N \| S(\chi^i) - \chi^i \| ^2 \quad (10)$$

The χ^i serves a dual purpose. Firstly, it is used as a location indicator of the mobile device for the signal prediction $S(\chi^i)$. Secondly, it acts as the true RF signal received by the AP.

F. Soft-landing Reconfiguration Algorithm

Once RIS-NeRF² has been adequately trained, it becomes a powerful tool for identifying the ideal configurations of our MetaMosaic. In its operational phase, the AP initiates a CSI measurement χ from the device. With the capabilities of RIS-NeRF², we can predict the final RF signal, $S_{AP}(\chi)$, that the AP receives. This signal is composed of three distinct components:

$$S_{AP}(\chi) = S_{LOS}(\chi) + S_{ENV}(\chi) + S_{RIS}(\chi) = S_{TRUNK}(\chi) + S_{RIS}(\chi)$$

where S_{LOS} denotes the signal that traverses the LoS path, S_{ENV} represents signals from uncontrollable environmental reflections, S_{TRUNK} is the sum of the LoS signal, and the uncontrollable reflection signals, and S_{RIS} originates from all unit cells of the RIS. Given that the positions of the RIS unit cells are known, we can further trace S_{RIS} as:

$$S_{RIS}(\chi) = \sum_{V_i \in \mathcal{V}_{RIS}} S(\chi, V_i) \quad (11)$$

with \mathcal{V}_{RIS} being the collection of all RIS unit cells and $S(\chi, V_i)$ calculated using Eqn. 7. Subsequently, we can deduce:

$$S_{TRUNK}(\chi) = S_{LOS}(\chi) + S_{ENV}(\chi) = S_{AP}(\chi) - S_{RIS}(\chi) \quad (12)$$

The unalterable trunk signal is assumed to be the primary contributor to the final signal. It is either strengthened or attenuated by the RIS unit cells. As shown in Fig. 8(a), RIS reflections have the potential to either boost or reduce the trunk signal, which depends on their phase relationship. Therefore, our configuration strategy is quite straightforward:

if the reflection from a unit cell $S(\chi, V_i)$ aligns in phase with the primary trunk signal, its reflective coefficient is maintained, i.e., $\Gamma(V_i) = 1$. If not, the coefficient is inverted, i.e., $\Gamma(V_i) = -1$. The outcomes of applying this configuration strategy are illustrated in Fig. 8(b).

IV. IMPLEMENTATION

The MetaMosaic architecture includes unit cells, surfaces, an RIS controller, and RIS-NeRF².

(1) Unit Cells: At its core is the EM4325 RFID chip [7], paired with a dual-frequency patch antenna. The reflection coefficient is managed using the BF1118 MOSFET [11]. Fig. 2(a) and (b) show the completed unit cells. The final PCB is produced using FR4 material with a thickness of 1.6mm, offering a cost-effective solution. The resonance frequency bandwidth ($> -3\text{dB}$) ranges from 2.403GHz to 2.531GHz, which cover the WiFi spectrum. Each cell is composed of an RFID chip (\$0.26), a MOSFET (\$0.19), two resistors (\$0.00051 each), two capacitors (\$0.0064 each), and two inductors (\$0.00019 each), totaling \$0.4759 per unit. With large-scale production, these costs are expected to decrease to a tenth of the current amounts. A total of 2,418 unit cells are prototyped for debugging and testing.

(2) Surfaces. To facilitate the evaluation in different scenes, we constructed six RISs by mounting unit cells in a grid pattern on movable planes, as illustrated in Fig. 2(c) and (d). Each surface comprises 13×31 unit cells and measures $1.2 \times 2\text{m}^2$. To visually indicate active unit cells, an ultra-low-power LED is integrated between the switch and the reflector. As shown in Fig. 2(e), the illuminated unit cells, distinguishable by their activated LEDs, represent those selected for engaging the phase-reversed reflections.

(3) Controller: The control mechanism in MetaMosaic essentially employs a standard ImpinJ R410 RFID reader [12] equipped with a 9dB directional antenna. The reader is connected through cables and manipulated through LLRP [13]. To activate the EM4325 chip's select state output through the AUX pin, it is necessary to modify two internal registers of the RFID chips, namely the I/O control word and the power management word, through the Write commands. Once these adjustments are made, all cells will consistently hook the Select events until they are powered down or unselected.

(4) RIS-NeRF². Our setup mirrors the configuration used in NeRF² [10], with specific adaptations. The voxel dimension is fixed at 1/8 of the wavelength. We set the batch size to 4096. The Adam optimizer [14] is employed for this process. The initial learning rate is established at $3e^{-4}$, which is then progressively reduced to $3e^{-5}$ through an exponential decay over the optimization period. We retain the default settings for other hyper-parameters, such as $\beta_1 = 0.9$, $\beta_2 = 0.999$, and $\varepsilon = 10^{-7}$. Typically, training the network for a single scene takes approximately 300 to 500k iterations to achieve convergence, using a single NVIDIA 3080Ti GPU, which roughly translates to a duration of about four hours. Nonetheless, the execution of interference is expedited, taking less than 10ms.

V. EXPERIMENTAL RESULTS

We now evaluate the performance of MetaMosaic and verify its capability to improve WiFi communication.

A. Performance of RIS-NeRF²

The principle innovation of MetaMosaic is the adoption of a neural radiance field, which greatly enhances the speed of evaluating reconfiguration strategies' effectiveness. Consequently, our evaluation centers on the accuracy of RIS-NeRF² in predicting signal strength. The precision of the radiance field model is deeply connected to the environment's specific setup, requiring tailored models for each scene. For this purpose, we collected a comprehensive dataset from 284,124 positions across ten varied scenes, as shown in Fig. 10. The six MetaMosaic surfaces were installed near the WiFi Access Point (AP), and mobile devices were relocated during the experiments.

(1) Accuracy: As standard procedures, we partitioned the dataset for each environment into two parts: allocating 80% for training purposes and reserving 20% for testing. To gauge the precision of our predictive model, we calculate the deviation, which quantifies the percentage discrepancy between predicted power and actual ground truth. A smaller deviation percentage reflects a prediction that more accurately mirrors the ground truth. The results of this methodical testing are illustrated in Fig 11. Analysis of the data reveals that in line with the NeRF², the prediction precision of MetaMosaic is exceptionally high, exhibiting an average median deviation of 0.74%; the median deviation remains below 1% for 90% of the scenes, with Scene A being the sole exception; Scene A exhibits a deviation of 2.25%, which is notably higher due to its lower density of data points compared to other scenarios. This experiment confirms the efficacy of RIS-NeRF² in the domain of channel modeling and prediction, thereby laying the groundwork for an informed reconfiguration strategy.

(2) Response Time: We conducted time measurements for reconfigurations at 50 different positions within Scenes A, B, C, and D. The CDFs of are depicted in Fig. 13. The durations recorded were 114ms, 97ms, 160ms, and 49ms for each scene, respectively. The primary factor contributing to these delays is the issuance of one or more Select commands, each taking about 0.825ms. The rapid response time of our system is a crucial aspect, particularly in dynamic environments where conditions change frequently. In contrast, the response times for the SOTA solutions (like RFocus [2]) are usually 1-10 seconds [2], [15], [4]. Their longer durations are a consequence of their hard-landing strategy, which requires substantial time to gather feedback from mobile devices. In comparison, our approach necessitates only one-tenth of this time, significantly enhancing response efficiency.

B. Overall Performance

Finally, we evaluate the overall performance of MetaMosaic from a complete system perspective.

(1) Gain across Scenes. To assess the overall enhancement provided by MetaMosaic, we deployed the six surfaces in the

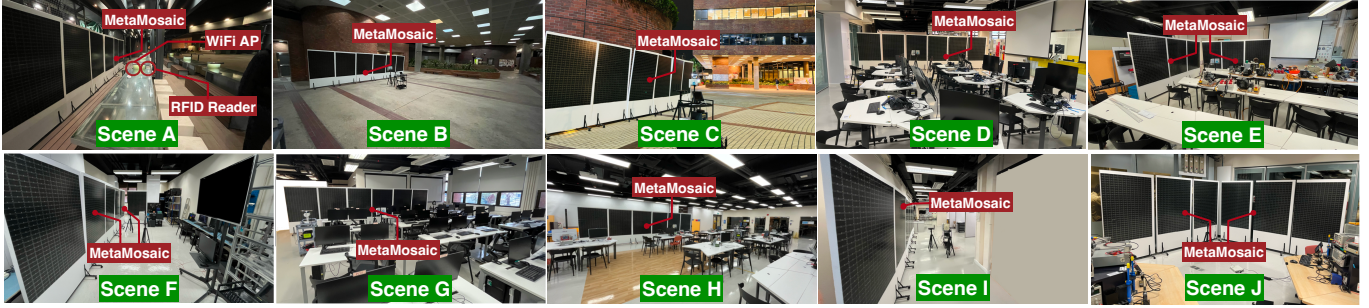


Fig. 10: Illustration of Experimental Scenes

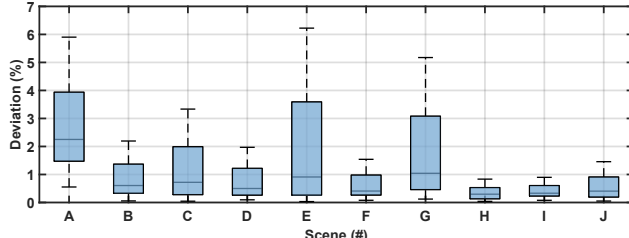


Fig. 11: Accuracy of RIS-NeRF²

ten scenes and conducted evaluations at 50 random distinct positions within each scene to gauge the system's efficacy. The gain was calculated as the decibel (dB) ratio of signal strength with versus without reflection adjustments. The experimental results are shown in Fig. 12. From the figure, we have the following insights: MetaMosaic consistently enhances signal strength at WiFi terminals, with an average median gain of 18.82dB across all scenes; the highest median gain observed is 25dB (i.e., 316×) in Scene B (least uncontrollable reflections), whereas the lowest median gain recorded is 13.7dB in Scene J; the level of improvement is comparable in both semi-indoor and full-indoor settings, which validates the versatility of our methodology. These notable enhancements can be credited to two principal benefits of MetaMosaic. Firstly, the surfaces act as a fully-reflective RIS regardless of switch states, thereby generating an increased number of reflections. This is especially beneficial in semi-indoor settings where wall reflections are absent. Secondly, our meticulously developed configuration algorithms enable precise alignment of these reflections, substantially mitigating mutual cancellation.

(2) Comparison to SOTA Solution. Our study primarily compares MetaMosaic with RFocus [2], a large-scale, one-bit amplitude-reconfigurable RIS. Limited by the unavailability of similar hardware, our analysis focuses on the performance gains achievable through the reconfiguration algorithm in our RIS setup (i.e., phase modulation). RFocus utilizes a hard-landing strategy involving a voting mechanism, requiring 165 randomized iterations and feedback to determine the optimal states of its unit cells for each assessment. We benchmarked MetaMosaic against RFocus in four different scenarios: Scenes A, B, C, and D. The outcomes of this comparison are illustrated in Fig. 14. Notably, MetaMosaic demonstrates superior performance, achieving 10.02dB, 7.74dB, 4.60dB, 8.43dB, and 11.74dB higher median gains than RFocus in each respective scene. This superior performance of Meta-

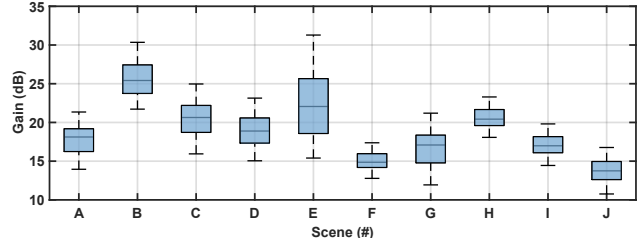


Fig. 12: Gain vs. scenario

Mosaic can be attributed to the advantages of its pre-learning model, RIS-NeRF², which ensures consistent and higher gains. Moreover, the results show that MetaMosaic typically follows Gaussian distributions, while RFocus displays more irregular patterns, resulting in a standard deviation that is 2.5dB higher than that of MetaMosaic. The inherent randomness in RFocus leads to relatively unstable gains in each iteration.

(3) Scalability. To assess the influence of varying the number of unit cells, we conducted experiments using different quantities of cells selected from three surfaces for reconfiguration while keeping the rest unchanged. Specifically, we tested with subsets of 600, 1,200, 1,800, and 2,400 cells out of a total of 2,418. The results are depicted in Fig. 15. As a result, a progressive increase in median gain: from 8.59dB with 600 cells to 13.12dB with 1200 cells, 18.51dB with 1800 cells, and 21.88dB with 2400 cells. This demonstrates that even with up to 25% of the RFID tags not being selected due to communication failures, the system's performance retains approximately 85% of its maximum capability. Such scalability ensures that MetaMosaic can effectively handle partial tag failures, thereby mitigating potential communication disruptions and enhancing the overall reliability of the network in complex channel conditions.

(4) Impact of Layout: The flexibility of MetaMosaic, enabled by discarding wired connections, allows for diverse configurations. In our tests, 186 unit cells were organized into linear, L-shaped, X-shaped, square, and random patterns to evaluate how different arrangements affect gain. According to results shown in Fig. 16, gain variations were minimal, within a 2dB range across layouts. The random pattern yielded the highest median gain of 4.29dB. This is because the random pattern may create a sparse array that provides a broader effective aperture. Irrespective of the unit cells' deployment pattern, an enhancement in performance was observed, showcasing MetaMosaic's versatile deployment capabilities.

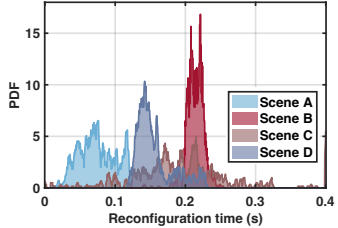


Fig. 13: Response Time

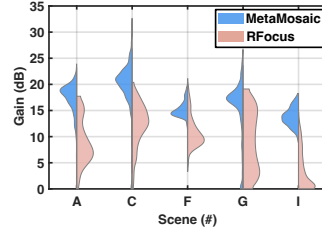


Fig. 14: RFocus vs. MetaMosaic

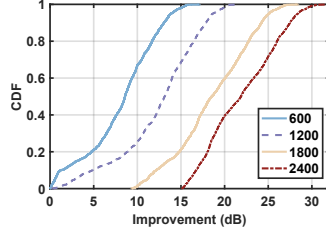


Fig. 15: Scalability

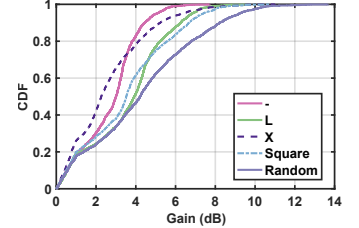


Fig. 16: Layout

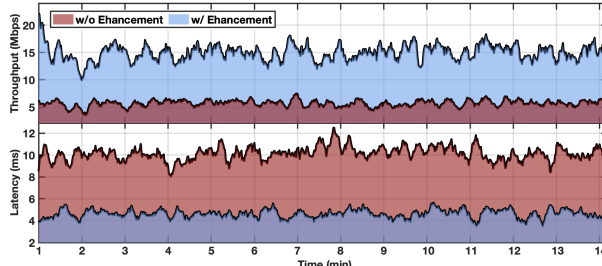


Fig. 17: Throughput and Latency in the Field Study

VI. FIELD STUDY: XR BOOSTER

Finally, we show how MetaMosaic enhances extended reality (XR) applications by enabling reliable, high-speed wireless communication, as shown in Fig. 2(e). In our setup, a PC in AP mode serves as the streaming source, sending data packets to a Hololens 2 headset [16] continuously. The headset user moves to various locations every 30 seconds. We employ `iperf` and `ping` tools to measure throughput and latency, respectively. Fig. 17 compares the performance with and without MetaMosaic’s enhancement over a 14-minute duration. The findings reveal average throughputs of 14.86 Mbps with RIS enhancement versus 5.66 Mbps without, marking a 2.6-fold increase. Additionally, latency is decreased from 10.07ms to 4.63ms, a reduction of 54%. According to a study by Ericsson, XR technologies necessitate network capabilities of tens of Mbps in bitrate and 10 - 20ms in latency for a high-quality user experience [17], benchmarks that our experiment successfully meets. Thus, we believe that MetaMosaic will emerge as a cost-efficient method to advance XR technologies without the need for protocol or hardware upgrades in communication systems.

VII. RELATED WORK

(1) RFID systems: In recent years, RFID systems have garnered great attention from the networking community [18], [19]. Many researchers have utilized RFID systems for localization [20], [21], [22], [23], image annotation [24], human activity sensing [25], [26], spectrum mapping [27], etc. Unlike them, MetaMosaic tries to use RFID systems as RISs, which can be further utilized in various fields, such as wireless communication [28], [15] and localization [29].

(2) RIS systems: RIS technology has been shown to effectively beamform electromagnetic waves to enhance link SNR by controlling amplitude [30], [31], [32], phase [33], [34], [35], and polarization [36]. Unlike passive metasurfaces [37], [38], [39], RIS enables real-time adaptability and

optimization of wavefront properties. Recently, one-bit RIS systems have gained prominence for balancing complexity and performance [15], [2], [40], yet they often rely on wired connections for power supply and state control, limiting their scalability and flexibility. A study closely related to our work is [41], which explores RFID systems for RIS control using specialized chips in a proof-of-concept unit cell. We further this idea by employing commercially available, cost-effective RFID chips for large-scale, low-cost production. While MetaSight [29] and IMS [42] utilize WISPs or RFIDs as transceivers of the whole surfaces with wired unit cells, our approach eliminates wired connections entirely, using RFID tags as independent, battery-free unit cells. This greatly enhances scalability and flexibility, pushing the boundaries of RIS system design.

(3) Neural Channel Representation: The advent of NeRF [9] has significantly sparked interest beyond the computer vision field [43], [44]. There has been a successful application of NeRF in wireless systems [10], [45], [46], [47]. A notable example is NeRF², which extends NeRF from optical to electromagnetic waves, for accurate channel prediction. Qualcomm’s WiNeRT [45] employs neural representation to simulate ray-surface interactions, aiding in the estimation of RF signal propagation along transmit-receive paths.

VIII. CONCLUSION

This paper introduces MetaMosaic, a novel reconfigurable intelligent surface system utilizing cost-effective RFID tags for enhanced wireless communication. Our system, unique for its scalability and flexibility, significantly surpasses existing RIS solutions in signal enhancement and throughput improvement, thanks to its innovative use of battery-free, RFID-addressed unit cells. This work establishes a new benchmark in RIS technology, paving the way for future innovations in intelligent and responsive wireless network environments. In the future, we can enhance the adaptability of RIS-NeRF² in dynamic scenarios through incremental learning and leverage transfer learning methods that enable the reuse of RIS-NeRF² in diverse scenarios.

ACKNOWLEDGEMENT

This work is supported by UGC/GRF (No. 15211024, 15215421), Innovation and Technology Fund (GHP/079/22SZ, ITS/034/23FP), and Shenzhen Fundamental Research Scheme (No. JCYJ20230807140410022). We thank all the anonymous reviewers for their valuable comments and helpful suggestions.

REFERENCES

- [1] S. Gong, X. Lu, D. T. Hoang, D. Niyato, L. Shu, D. I. Kim, and Y.-C. Liang, “Toward smart wireless communications via intelligent reflecting surfaces: A contemporary survey,” *IEEE Communications Surveys & Tutorials*, vol. 22, no. 4, pp. 2283–2314, 2020.
- [2] V. Arun and H. Balakrishnan, “Rfocus: Beamforming using thousands of passive antennas,” in *Proc. of USENIX NSDI*, 2020, pp. 1047–1061.
- [3] C. Liu, F. Yang, S. Xu, and M. Li, “Reconfigurable metasurface: A systematic categorization and recent advances,” *arXiv preprint arXiv:2301.00593*, 2023.
- [4] L. Chen, W. Hu, K. Jamieson, X. Chen, D. Fang, and J. Gummesson, “Pushing the physical limits of {IoT} devices with programmable metasurfaces,” in *Proc. of USENIX NSDI*, 2021, pp. 425–438.
- [5] “RFID Forecasts, Players and Opportunities 2023-2033,” <https://www.idtechex.com/en/research-report/rfid-forecasts-players-and-opportunities-2023-2033/927>, 2023.
- [6] “EPC Gen2, EPCglobal.” www.gs1.org/epcglobal.
- [7] EM Microelectronic, “EPC and UHF ICs - EM4325,” <https://www.emmicroelectronic.com/product/epc-and-uhf-ics/em4325>, 2023.
- [8] A. Sayanskiy, A. Belov, R. Yafasov, A. Lyulyakin, A. Sherstobitov, S. Glybovski, and V. Lyshev, “A 2d-programmable and scalable reconfigurable intelligent surface remotely controlled via digital infrared code,” *IEEE Transactions on Antennas and Propagation*, vol. 71, no. 1, pp. 570–580, 2022.
- [9] B. Mildenhall, P. P. Srinivasan, M. Tancik, J. T. Barron, R. Ramamoorthi, and R. Ng, “Nerf: Representing scenes as neural radiance fields for view synthesis,” in *European conference on computer vision*. Springer, 2020, pp. 405–421.
- [10] X. Zhao, Z. An, Q. Pan, and L. Yang, “Nerf²: Neural radio-frequency radiance fields,” *arXiv preprint arXiv:2305.06118*, 2023.
- [11] NXP, “BF1118,” https://www.nxp.com/part/BF1118R#, 2023, accessed: 2024-01-01.
- [12] “Impinj, Inc.” <http://www.impinj.com/>.
- [13] EPCglobal, “Low level reader protocol (llrp),” 2010.
- [14] D. P. Kingma and J. Ba, “Adam: A method for stochastic optimization,” *arXiv preprint arXiv:1412.6980*, 2014.
- [15] C. Feng, X. Li, Y. Zhang, X. Wang, L. Chang, F. Wang, X. Zhang, and X. Chen, “Rflens: metasurface-enabled beamforming for iot communication and sensing,” in *Proc. of ACM MobiCom*, 2021.
- [16] “Hololens,” <https://www.microsoft.com/en-us/hololens>, 2024.
- [17] Ericsson, “Future network requirements for xr apps,” n.d.
- [18] X. Fan, H. Ding, S. Li, M. Sanzari, Y. Zhang, W. Trappe, Z. Han, and R. E. Howard, “Energy-ball: Wireless power transfer for batteryless internet of things through distributed beamforming,” *Proc. of ACM IMWUT*, vol. 2, no. 2, pp. 1–22, 2018.
- [19] D. Dai, Z. An, Z. Gong, Q. Pan, and L. Yang, “[RFID+]: Spatially controllable identification of {UHF}{RFIDs} via controlled magnetic fields,” in *21st USENIX Symposium on Networked Systems Design and Implementation (NSDI 24)*, 2024, pp. 1351–1367.
- [20] L. Dodds, I. Perper, A. Eid, and F. Adib, “A handheld fine-grained rfid localization system with complex-controlled polarization,” *arXiv preprint arXiv:2302.13501*, 2023.
- [21] T. Boroushaki, M. Lam, W. Chen, L. Dodds, A. Eid, and F. Adib, “Exploiting synergies between augmented reality and rfids for item localization and retrieval,” in *Proc. of IEEE RFID*, 2023, pp. 30–35.
- [22] B. Liang, P. Wang, R. Zhao, H. Guo, P. Zhang, J. Guo, S. Zhu, H. H. Liu, X. Zhang, and C. Xu, “[RF-Chord]: Towards deployable {RFID} localization system for logistic networks,” in *Proc. of USENIX NSDI*, 2023, pp. 1783–1799.
- [23] Y. Ma, N. Selby, and F. Adib, “Minding the billions: Ultra-wideband localization for deployed rfid tags,” in *Proc. of ACM MobiCom*, 2017, pp. 248–260.
- [24] E. Sie and D. Vasisht, “Rf-annotate: Automatic rf-supervised image annotation of common objects in context,” in *Proc. of IEEE ICRA*, 2022, pp. 2590–2596.
- [25] J. Wang, J. Li, M. H. Mazaheri, K. Katsuragawa, D. Vogel, and O. Abari, “Sensing finger input using an rfid transmission line,” in *Proc. of SenSys*, 2020, pp. 531–543.
- [26] J. Han, H. Ding, C. Qian, D. Ma, W. Xi, Z. Wang, Z. Jiang, and L. Shangguan, “Cbid: A customer behavior identification system using passive tags,” in *Proc. of IEEE ICNP*, 2014.
- [27] M. I. Ahmed, A. Bansal, K. Yuan, S. Kumar, and P. Steenkiste, “Battery-free wideband spectrum mapping using commodity rfid tags,” in *Proc. of ACM MobiCom*, 2023, pp. 1–16.
- [28] X. Li, C. Feng, X. Wang, Y. Zhang, Y. Xie, and X. Chen, “[RF-Bouncer]: A programmable dual-band metasurface for sub-6 wireless networks,” in *Proc. of USENIX NSDI*, 2023, pp. 389–404.
- [29] D. Xie, X. Wang, and A. Tang, “Metasight: localizing blocked rfid objects by modulating nlos signals via metasurfaces,” in *Proc. of MobiSys*, 2022, pp. 504–516.
- [30] L. Liu, X. Zhang, M. Kenney, X. Su, N. Xu, C. Ouyang, Y. Shi, J. Han, W. Zhang, and S. Zhang, “Broadband metasurfaces with simultaneous control of phase and amplitude,” *Advanced materials*, vol. 26, no. 29, pp. 5031–5036, 2014.
- [31] R. I. Zelaya, W. Sussman, J. Gummesson, K. Jamieson, and W. Hu, “Lava: fine-grained 3d indoor wireless coverage for small iot devices,” in *Proc. of ACM SIGCOMM*, 2021, pp. 123–136.
- [32] R. Ma, R. I. Zelaya, and W. Hu, “Softly, deftly, scrolls unfurl their splendor: Rolling flexible surfaces for wideband wireless,” *arXiv preprint arXiv:2306.02361*, 2023.
- [33] W. Tang, J. Y. Dai, M. Chen, X. Li, Q. Cheng, S. Jin, K.-K. Wong, and T. J. Cui, “Programmable metasurface-based rf chain-free 8psk wireless transmitter,” *Electronics letters*, vol. 55, no. 7, pp. 417–420, 2019.
- [34] Z. Li, Y. Xie, L. Shangguan, R. I. Zelaya, J. Gummesson, W. Hu, and K. Jamieson, “Towards programming the radio environment with large arrays of inexpensive antennas,” in *16th USENIX Symposium on Networked Systems Design and Implementation (NSDI 19)*, 2019, pp. 285–300.
- [35] J. Tong, Z. An, X. Zhao, S. Liao, and L. Yang, “In-sensor machine learning: Radio frequency neural networks for wireless sensing,” in *Proc. of ACM MobiHoc*, 2024, pp. 261–270.
- [36] Z. Wu, Y. Ra'di, and A. Grbic, “Tunable metasurfaces: A polarization rotator design,” *Physical Review X*, vol. 9, no. 1, p. 011036, 2019.
- [37] H. Pan, L. Qiu, B. Ouyang, S. Zheng, Y. Zhang, Y.-C. Chen, and G. Xue, “Pmsat: Optimizing passive metasurface for low earth orbit satellite communication,” in *Proceedings of the 29th Annual International Conference on Mobile Computing and Networking*, 2023, pp. 1–15.
- [38] A. Pallaprolu, W. Hurst, S. Paul, and Y. Mostofi, “I beg to diffract: Rf field programming with edges,” in *Proceedings of the 29th Annual International Conference on Mobile Computing and Networking*, 2023, pp. 1–15.
- [39] K. Qian, L. Yao, K. Zheng, X. Zhang, and T. N. Ng, “Uniscatter: a meta-material backscatter tag for wideband joint communication and radar sensing,” in *Proceedings of the 29th Annual International Conference on Mobile Computing and Networking*, 2023, pp. 1–16.
- [40] K. W. Cho, M. H. Mazaheri, J. Gummesson, O. Abari, and K. Jamieson, “[mmWall]: A steerable, transreflective metamaterial surface for {NextG}{mmWave} networks,” in *20th USENIX Symposium on Networked Systems Design and Implementation (NSDI 23)*, 2023, pp. 1647–1665.
- [41] F. Lestini, G. Marrocco, and C. Occhiuzzi, “Feasibility of rfid-based control of reconfigurable intelligent surfaces (riss) for wireless communication systems,” in *2023 IEEE 13th International Conference on RFID Technology and Applications (RFID-TA)*. IEEE, 2023, pp. 241–244.
- [42] Z. X. Wang, C. K. Shen, J. W. Wu, H. Xu, Q. Cheng, T. T. Ye, and T. J. Cui, “A long-range and nearly passive rfid-controlled information metasurface,” *Advanced Optical Materials*, p. 2203114, 2023.
- [43] C. Chen, A. Richard, R. Shapovalov, V. K. Ithapu, N. Neverova, K. Grauman, and A. Vedaldi, “Novel-view acoustic synthesis,” in *Proc. of the IEEE/CVF CVPR*, 2023, pp. 6409–6419.
- [44] B. Attal, E. Laidlaw, A. Gokaslan, C. Kim, C. Richardt, J. Tompkin, and M. O’Toole, “Törf: Time-of-flight radiance fields for dynamic scene view synthesis,” *Advances in neural information processing systems*, vol. 34, pp. 26 289–26 301, 2021.
- [45] T. Orekondy, P. Kumar, S. Kadambi, H. Ye, J. Soriaga, and A. Behboodi, “Winert: Towards neural ray tracing for wireless channel modelling and differentiable simulations,” in *The Eleventh International Conference on Learning Representations*, 2022.
- [46] J. Hoydis, F. A. Aoudia, S. Cammerer, M. Nimier-David, N. Binder, G. Marcus, and A. Keller, “Sionna rt: Differentiable ray tracing for radio propagation modeling,” *arXiv preprint arXiv:2303.11103*, 2023.
- [47] X. Chen and X. Zhang, “Rf genesis: Zero-shot generalization of mmwave sensing through simulation-based data synthesis and generative diffusion models,” in *Proc. of ACM SenSys*, 2023.